

This is the accepted manuscript made available via CHORUS. The article has been published as:

Magnetic properties of $\text{Sr}_{\{3\}}\text{NiIrO}_{\{6\}}$ and $\text{Sr}_{\{3\}}\text{CoIrO}_{\{6\}}$: Magnetic hysteresis with coercive fields of up to 55 T

John Singleton, Jae Wook Kim, Craig V. Topping, Anders Hansen, Eun-Deok Mun, S. Chikara, I. Lakis, Saman Ghannadzadeh, Paul Goddard, Xuan Luo, Yoon Seok Oh, Sang-Wook Cheong, and Vivien S. Zapf

Phys. Rev. B **94**, 224408 — Published 8 December 2016

DOI: [10.1103/PhysRevB.94.224408](https://doi.org/10.1103/PhysRevB.94.224408)

Magnetic properties of $\text{Sr}_3\text{NiIrO}_6$ and $\text{Sr}_3\text{CoIrO}_6$: magnetic hysteresis with coercive fields of up to 55 T

John Singleton,^{1,2} Jae Wook Kim,¹ Craig V. Topping,^{1,2,3} Anders Hansen,¹ Eun-Deok Mun,^{1,4} S. Chikara,¹ I. Lakis,¹ Saman Ghannadzadeh,² Paul Goddard,⁵ Xuan Luo,^{6,7} Yoon Seok Oh,⁶ Sang-Wook Cheong,⁶ Vivien S. Zapf¹

¹*National High Magnetic Field Laboratory (NHMFL), MS E536,*

Los Alamos National Laboratory, Los Alamos, NM 87545, USA

²*University of Oxford, Department of Physics, The Clarendon Laboratory,*
Parks Road, Oxford, OX1 3PU, United Kingdom

³*Department of Chemistry, University of Edinburgh,*
Edinburgh, Midlothian EH8 9YL, United Kingdom

⁴*Department of Physics, Simon Fraser University, Burnaby, BC, V5A 1S6, Canada*

⁵*Department of Physics, University of Warwick,*
Gibbet Hill Road, Coventry, CV4 7AL, United Kingdom

⁶*RCEM & Dept. of Physics and Astronomy, Rutgers University, Piscataway, NJ 08854, USA and*

⁷*POSTECH, Pohang University of Science and Technology,*
San 31 Hyoja-dong, Nam-gu, Pohang-si, Gyungbuk, 790-784, Republic of Korea

We report extraordinarily large magnetic hysteresis loops in the iridates $\text{Sr}_3\text{NiIrO}_5$ and $\text{Sr}_3\text{CoIrO}_6$. We find coercive magnetic fields of up to 55 T with switched magnetic moments $\approx \mu_B$ per formula unit in $\text{Sr}_3\text{NiIrO}_6$ and coercive fields of up to 52 T with switched moments $\approx 3\mu_B$ per formula unit in $\text{Sr}_3\text{CoIrO}_6$. We propose that the magnetic hysteresis involves the field-induced evolution of quasi-one-dimensional chains in a frustrated triangular configuration. The striking magnetic behaviour is likely to be linked to the unusual spin-orbit-entangled local state of the Ir^{4+} ion and its potential for anisotropic exchange interactions.

I. INTRODUCTION

Oxides containing $5d$ ions, particularly Ir^{4+} , offer new possibilities for novel spin-orbit and spin-lattice coupling effects. In these materials, the energy scales for spin-orbit interactions, Coulomb repulsion, and crystalline-electric fields can be very similar¹. This unusual situation, in comparison to analogous $3d$ oxides, results from a decrease in the strength of correlation effects and an increase in spin-orbit interactions as one descends the periodic table². Usually, the Coulomb repulsion and spin-orbit interactions are responsible for Hund's rules that determine the ground states of magnetic ions. However, in certain $5d$ (and some $4d$) oxides, the competition between the three similar energy scales can result in exotic magnetic states such as spin-orbit entanglement, extreme magnetic exchange anisotropy leading to *e.g.* Kitaev spin liquids, and spin-orbit entangled Mott insulating behaviour^{1,3-9}. In this paper, we report extremely large coercive magnetic fields of up to 55 T in $\text{Sr}_3\text{NiIrO}_6$ and 52 T in $\text{Sr}_3\text{CoIrO}_6$, with switched magnetic moments $\approx \mu_B$ and $3\mu_B$ per formula unit, respectively. This large hysteresis evolves out of a frustrated, antiferromagnetic ground state that incorporates an entangled spin-orbit state on the $5d$ ion¹⁰.

$\text{Sr}_3\text{NiIrO}_6$ and $\text{Sr}_3\text{CoIrO}_6$ are members of the $\text{A}_3\text{BB}'\text{O}_6$ family, where A is an alkaline earth and B and B' are transition metal ions¹¹. Soon after their synthesis¹², it was realized^{13,14} that the interplay of electron correlations, magnetic frustration, reduced dimensionality and magnetocrystalline anisotropy could lead to interesting physics; subsequently the structural and magnetic properties have been the subject of several studies (*e.g.*

Refs. [13–18]). The salient structural details^{11,13,15,18} are shown in Fig. 1(a) and (b) for $\text{Sr}_3\text{NiIrO}_6$. The Ni^{2+} and Ir^{4+} magnetic ions occupy oxygen cages that alternate in chains parallel to the c -axis [Fig. 1(a)]. These chains are in turn arranged in a hexagonal pattern in the ab -plane [Fig. 1(b)]¹³. Ni^{2+} is surrounded by a trigonal bipyramid of oxygen atoms, while the Ir^{4+} ion sits in distorted octahedral oxygen cage^{11,13,18}. Magnetic frustration is intrinsic to such a structure, and can result from antiferromagnetic interactions within the triangular lattice in the ab -plane, and from frustration between nearest-neighbor and next-nearest neighbor interactions along the c -axis chains^{11,14,19-21}. Experimentally, this is manifested in the complex behavior of the magnetic susceptibilities of $\text{Sr}_3\text{CoIrO}_6$ [15 and 16] and $\text{Sr}_3\text{NiIrO}_6$ [13, 15–17], and their structurally similar relatives $\text{Ca}_3\text{CoRhO}_6$ [22] and $\text{Sr}_3\text{NiRhO}_6$ [23]; below a temperature conventionally¹⁵ labeled T_1 , the susceptibility rises strongly; at a temperature T_2 , a factor $\approx 3-5$ lower than T_1 , the spin dynamics are frozen in, and slow relaxation of magnetic properties¹⁷ is observed. (As will be shown in Section III B below, the samples used in the current study behave in a very similar way.) However, no heat capacity signature of the magnetic ordering has been observed in either $\text{Sr}_3\text{NiIrO}_6$ or $\text{Sr}_3\text{CoIrO}_6$, suggesting a gradual onset of partially disordered magnetism^{16,17}. Moreover, no structural change was seen at either T_1 or T_2 [13 and 15].

In conjunction with the magnetization results, neutron-scattering data for the low-temperature phases of $\text{Sr}_3\text{NiIrO}_6$ and $\text{Sr}_3\text{CoIrO}_6$ have been interpreted either in terms of amplitude-modulated antiferromagnetism or as a partially-disordered antiferromagnetic (PDA) state^{15,16}. Such PDA states, proposed by

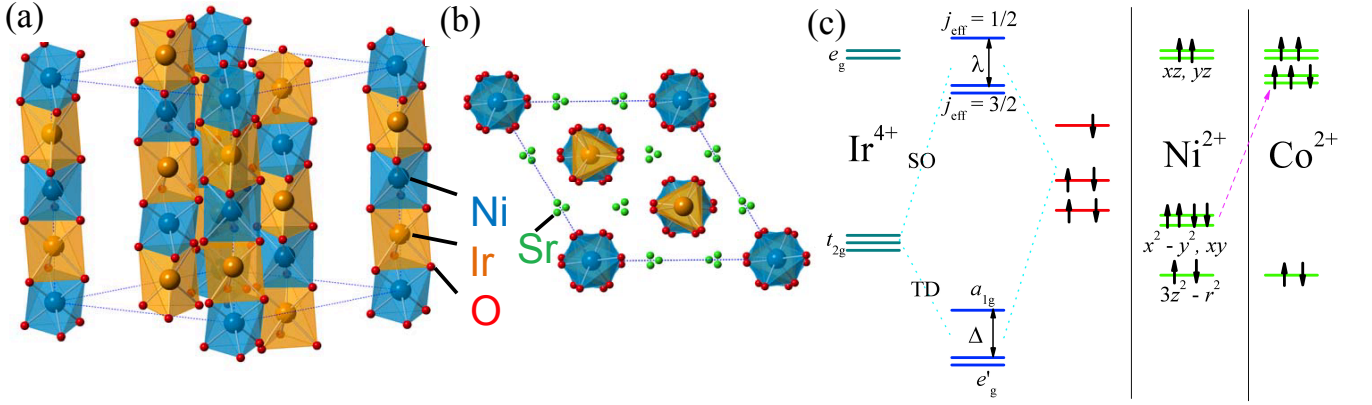


FIG. 1. The crystal structure of $\text{Sr}_3\text{NiIrO}_6$ as viewed from the (a) [110] and (b) [001] directions^{11,13,15,18}. The Ni^{2+} and Ir^{4+} ions occupy oxygen trigonal bipyramids (blue) and distorted oxygen octahedra (orange), respectively. For clarity, Sr ions are not shown in (a). ($\text{Sr}_3\text{CoIrO}_6$ is isostructural to $\text{Sr}_3\text{NiIrO}_6$.) (c) Schematic level diagrams for Ir^{4+} (after Ref. [10]), Ni^{2+} , and Co^{2+} (based on Refs. [10, 19–21]). Ir^{4+} t_{2g} and e_g levels split by the octahedral environment are shown in dark green; dark blue levels show schematically the effects of the trigonal distortion (TD- splitting the states by Δ) and spin-orbit coupling (SO- splitting the states by λ). These similarly sized effects result in spin-orbit entangled Ir^{4+} levels (red- not to scale), derived predominantly from t_{2g}^5 configurations, with a relatively small $t_{2g} - e_g$ mixing; Electron spins are shown as black arrows: the effective spins are $S = 1$ for Ni^{2+} and $S = \frac{3}{2}$ for Co^{2+} .

Mekata²⁴, were first reported for the $\text{A}_3\text{BB}'\text{O}_6$ family in Ref. 25. The PDA arrangement proposed for $\text{Sr}_3\text{NiIrO}_6$ and $\text{Sr}_3\text{CoIrO}_6$ involves the magnetic moments of two ferrimagnetic c -axis chains being antiparallel to each other, whilst the moments on the third chain are disordered^{15,16,26}; sometimes the latter chain is referred to as “paramagnetic”.

Three groups performed *ab-initio* electronic structure calculations on $\text{Sr}_3\text{NiIrO}_6$, confirming that it is a Mott-insulating state with relatively large moments on the magnetic ions^{19–21}, but disagreeing about the nature of the $5d$ electronic levels, the sign of the nearest-neighbor Ni-Ir interactions, and the magnetocrystalline anisotropy¹⁰. Besides the frustration inherent to the structure, the behavior of $\text{Sr}_3\text{NiIrO}_6$ and $\text{Sr}_3\text{CoIrO}_6$ is further complicated by spin-orbit entanglement¹⁰ of the kind first observed in Sr_2IrO_4 [1 and 27]. In the latter compound, the magnetic wavefunction is referred to as a $J_{\text{eff}} = \frac{1}{2}$ state, where J_{eff} is an effective total angular momentum. However, as already noted, compared to Sr_2IrO_4 , which has an octahedral oxygen cage around the Ir^{4+} ion^{1,27}, the oxygen cages in $\text{Sr}_3\text{NiIrO}_6$ and $\text{Sr}_3\text{CoIrO}_6$ are trigonally distorted^{11,13,18}. Recently, resonant inelastic X-ray scattering (RIXS) measurements were combined with electronic-structure calculations incorporating non-cubic crystal-field effects and spin-orbit coupling¹⁰; these calculations (see schematic in Fig. 1(c), left-hand side) show that for $\text{Sr}_3\text{NiIrO}_6$, the trigonal distortion and the spin-orbit coupling possess similar energy scales. Consequently, the final wavefunction departs from the “pure” $J_{\text{eff}} = \frac{1}{2}$ state due to the non-cubic environment¹⁰. The resulting spin-orbit entangled ground state produces a strong Ising anisotropy of the Ir-Ni exchange interactions, shown in the analysis of spin-wave excita-

tions observed in RIXS and neutron scattering¹⁰. This uniaxial anisotropy competes with a strong Ni^{2+} single-ion easy-plane anisotropy¹⁰. Neutron-scattering experiments by the same group found an apparent Ir^{4+} moment of $0.5\mu_B$ [15], a value used to constrain the electronic-structure calculations¹⁰. The Ni^{2+} spin in $\text{Sr}_3\text{NiIrO}_6$ is found to be close to $S = 1$, with a small orbital contribution¹⁰; overall, the moment contributed by each Ni^{2+} is around $1.5\mu_B$ [15] [Fig. 1(c)].

$\text{Sr}_3\text{CoIrO}_6$ has been subjected to slightly less scrutiny; it is thought that the Co^{2+} is in the $S = \frac{3}{2}$ configuration with a significant orbital contribution [Fig. 1(c)]²¹. The total Co^{2+} moment has been calculated to be $4.3\mu_B$ with a strong Ising anisotropy along the c -axis²¹, whilst a neutron diffraction study¹⁶ estimates the ordered Co^{2+} moment to be $3.6\mu_B$ per ion.

Having summarized the background to our study, the rest of the paper is organized as follows. Sample growth and other experimental details are described in Section II; given that the hysteretic behavior in our iridates evolves within a state that exhibits slow relaxation of magnetism, we pay particular attention to the *timescales* of the measurement techniques employed. The large coercive fields and hysteresis loops are described in Section III A; III B shows related low-field magnetic properties, including the previously reported emergence of sluggish kinetics at temperatures well below antiferromagnetic ordering, whilst Section III C investigates the sample-history dependence of the hysteresis loops. A detailed discussion of the evolution of the low-temperature magnetic groundstates of $\text{Sr}_3\text{NiIrO}_6$ and $\text{Sr}_3\text{CrIrO}_6$ with magnetic field follows in Section IV, whilst conclusions are given in Section V.

II. EXPERIMENTAL METHODS

A. Sample growth

Polycrystalline $\text{Sr}_3\text{NiIrO}_6$ and $\text{Sr}_3\text{CoIrO}_6$ were prepared through solid-state reaction at 1300°C . The polycrystalline samples used for magnetization measurements took the form of solid blocks; powders were not used, to avoid the problem of individual grains rotating in high fields. Single crystals of $\text{Sr}_3\text{NiIrO}_6$ were grown using K_2CO_3 as flux. The single crystals are hexagonal plates with typical dimensions $2 \times 2 \times 0.5 \text{ mm}^3$. Powder X-ray data are shown in the Supplementary Information²⁸.

B. Magnetization measurements

Magnetization versus field and temperature in quasi-static fields were measured with a DC SQUID in a 7 T superconducting magnet (MPMS, Quantum Design) and a vibrating-sample magnetometer (VSM) in a superconducting magnet (PPMS-14, Quantum Design). AC susceptibility data were measured with an AC SQUID in a 7 T superconducting magnet, and an AC susceptometer in a 14 T superconducting magnet, both by Quantum Design.

The pulsed-field magnetization experiments used a 1.5 mm bore, 1.5 mm long, 1500-turn compensated-coil susceptometer, constructed from 50-gauge, high-purity copper wire²⁹. When a sample is within the coil, the signal is $V \propto (dM/dt)$, where t is the time. Numerical integration is used to evaluate M . The susceptometer was placed within ^3He cryostats providing temperatures down to 0.4 K. Samples were mounted within a 1.3 mm diameter ampoule that can be moved in and out of the coil. Accurate values of M are obtained by subtracting empty-coil data from those measured under identical conditions with the sample present. The pulsed-field data are calibrated by scaling to data measured in a PPMS VSM at temperatures above the onset of hysteresis and sweep-rate dependence, which is 25 K for $\text{Sr}_3\text{NiIrO}_6$ and $\approx 60 \text{ K}$ for $\text{Sr}_3\text{CoIrO}_6$ (see Section III B below).

Pulsed fields were provided by a 65 T short-pulse magnet energized by a 4 MJ capacitor bank, or the generator-driven 60 T Long-Pulse Magnet at NHMFL Los Alamos³⁰; the field versus time profiles for these two magnets are shown in Figure 2. Measurements to 92 T were also performed in the capacitor-and-generator-driven 100 T Multi-shot Magnet³⁰. In all pulsed-field measurements, $\mu_0 H$ was measured by integrating the voltage induced in a ten-turn coil calibrated by observing the de Haas-van Alphen oscillations of the belly orbits of the copper coils of the susceptometer²⁹.

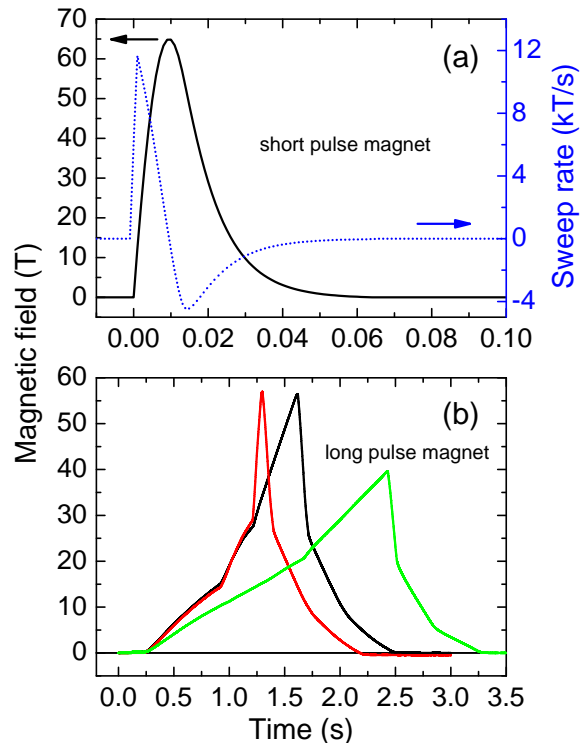


FIG. 2. Time dependence of magnetic fields for (a) a capacitor-bank-driven 65 T short-pulse magnet and (b) three examples of the controlled sweep patterns possible with the generator-driven 60 T Long Pulse Magnet. In (a), $\mu_0 dH/dt$ for the short-pulse magnet is shown in blue (right axis). In (b), the three stages in each of the field-sweep patterns are due to three separate coils that are energized in sequence by the generator.

C. Hysteresis loop measurement

In measuring hysteresis loops in pulsed fields, the initial field sweep (up and down) is performed after zero-field cooling from room temperature. Subsequent pulses are delivered approximately 45 minutes later (the cooling time of the magnet in question) while maintaining constant sample temperature. Given that M is obtained in the pulsed-field susceptometer by integrating dM/dt , the starting value $M(H = 0)$ is inferred from the hysteretic behaviour, which was observed to be similar to that of ferromagnetic hysteresis loops³¹. A jump in M is seen when magnetic field is swept up after zero-field cooling, no jump is seen as the field is swept down, and a negative jump twice as large is observed if the field is subsequently swept in the reverse direction. However, no jump is observed if the magnetic field is swept a second time in the same direction. If $M(H)$ for a given temperature and sample behaves the same regardless of field and temperature history we infer a lack of hysteresis and a loss of remanent magnetization.

III. RESULTS

A. Large coercive fields

Magnetic hysteresis loops in applied magnetic fields are plotted in Fig. 3 for single-crystal samples S2, S3, S4 of $\text{Sr}_3\text{NiIrO}_6$, polycrystalline sample P2 of $\text{Sr}_3\text{NiIrO}_6$, and polycrystalline sample P4 of $\text{Sr}_3\text{CoIrO}_6$. The data shown in Fig. 3 are measured in the 65 T short-pulse magnet (Fig. 2). Each loop is recorded using a succession of positive and negative field sweeps with an approximate 45 minute wait time in between. Samples are subjected to zero-field-cooling (ZFC) from above the hysteresis onset temperature (see below) before each hysteresis loop. All of the samples show a sharp jump in the magnetization between 34 and 55 T at low temperatures. We refer to the field position of the jump as the coercive field H_c (even if it is superimposed on a sloping background), since it bounds a hysteresis loop that extends from positive to negative applied fields with a remanent magnetization at $H = 0$. H_c is largest immediately after ZFC, and lower for subsequent field sweeps; the highest coercive field after ZFC [Fig. 3(d)] is 55 T. The maximum magnetization jump at H_c is $\approx \mu_B$ for $\text{Sr}_3\text{NiIrO}_6$, and $3\mu_B$ for $\text{Sr}_3\text{CoIrO}_6$, consistent with the larger Co^{2+} moment. We have also measured the magnetization of $\text{Sr}_3\text{NiIrO}_6$ sample S3 up to 92 T in the 100 T Multi-shot Magnet at NHMFL Los Alamos³⁰, and we find no additional sharp features in $M(H)$ beyond the coercive field.

Whilst all samples show high-field jumps, the behaviour of $M(H)$ away from the coercive field falls into two categories, even among samples from the same growth batch. In Figs. 3(a) and (d), ($\text{Sr}_3\text{NiIrO}_6$ S2 and P2) $M(H)$ shows a decreasing gradient approaching the coercive field on the up-sweep; a similar shape for $M(H)$ is seen approaching $H = 0$ on the down-sweep. However in Figs. 3(b) and (c), $\text{Sr}_3\text{NiIrO}_6$ samples S3 and S4 show a hysteresis loop superimposed on an almost linear $M(H)$ background. A similar sloping background $M(H)$ is observed for $\text{Sr}_3\text{CoIrO}_6$ P4 [Fig. 3(e)].

The variability of $M(H)$ below the coercive field is quite significant for samples within the same growth batch that otherwise show comparable X-ray diffraction patterns and (optical) surface quality. This suggests that the responsible defects and/or microstructures are of small - even nanometre - scale; one possibility is that small variations in oxygen stoichiometry within the same crystal batch affect the behaviour¹⁴. This is very suggestive of magnetic frustration, where the magnetic properties can be dramatically sensitive to small changes in stoichiometry; similar stoichiometry dependences of magnetic properties have been observed in isostructural family members, particularly $\text{Ca}_3\text{CoMnO}_6$ [32].

All but one of our $\text{Sr}_3\text{NiIrO}_6$ samples show remanent magnetization at $H = 0$ for at least 30 hours (the time limit of the experiment). Sample S2 (a tiny single crystal with optically perfect faces) is the exception; it exhibits remanent magnetization that relaxes on millisecond time

scales [Fig. 3(a)]. For $\text{Sr}_3\text{CoIrO}_6$ P4, part of the magnetization relaxes by the end of the pulse and between 10 and 50% of the remanent magnetization, depending on temperature, is retained on hour timescales.

The anisotropy of the magnetic hysteresis with respect to applied magnetic field direction for $\text{Sr}_3\text{NiIrO}_6$ is illustrated in Figs. 3(b) and (c). Here $M(H)$ of single crystals S3 and S4 is shown for both $\mathbf{H} \parallel \mathbf{c}$ and $\mathbf{H} \perp \mathbf{c}$. For $\mathbf{H} \perp \mathbf{c}$, no jump in M nor hysteresis is observed. Remarkably, despite the large coercive field, the magnetization is nearly isotropic at 60 T; at this field, the ratio between the magnitude of M for $\mathbf{H} \perp \mathbf{c}$ and M for $\mathbf{H} \parallel \mathbf{c}$ is 2/3 for sample S3, and 5/6 for sample S4. The magnetization would be approximately isotropic if the magnetic hysteresis between up and down sweeps were removed for $\mathbf{H} \parallel \mathbf{c}$. Interestingly, both single and polycrystals show similar size jumps in H_c . This is not expected if the polycrystalline data are simply an average of different single crystal orientations, and thus our data imply cooperative interactions among grains of different orientations.

The temperature dependences of $M(H)$ hysteresis loops are illustrated in Figs. 3(a), (b) for $\text{Sr}_3\text{NiIrO}_6$, and (e) for $\text{Sr}_3\text{CoIrO}_6$. The shift of H_c with T is given in more detail in Fig. 3(f), which shows the coercive fields for $\text{Sr}_3\text{NiIrO}_6$ samples S2 and S3, and $\text{Sr}_3\text{CoIrO}_6$ sample P4; H_c decreases linearly with increasing T for all samples, extrapolating to zero at 25 ± 1 K for $\text{Sr}_3\text{NiIrO}_6$ and 57 ± 4 K for $\text{Sr}_3\text{CoIrO}_6$. We will return to the significance of these temperatures in Section III B. At this point, we note that a coercive field $\mu_0 H_c \approx 22$ T was measured by another group in polycrystalline samples of $\text{Sr}_3\text{NiIrO}_6$ at $T = 15$ K [17]. This is similar to the values observed in our single-crystal samples at 15 K [see Figure 3(f)].

Turning to the temperature dependence of $M(H)$ in $\text{Sr}_3\text{NiIrO}_6$ for $\mathbf{H} \perp \mathbf{c}$ [Fig. 3(b)], no hysteresis is observed (as mentioned above), and M for $T < 25$ K is suppressed compared to the value at 25 K, consistent with overall antiferromagnetic exchange interactions^{10,13,15,17}.

B. Temperature-dependent magnetization

Magnetic susceptibility versus temperature, measured in superconducting magnets, is shown for different samples of $\text{Sr}_3\text{NiIrO}_6$ and $\text{Sr}_3\text{CoIrO}_6$ in Figs. 4(a) and (b). The difference between zero-field cooled and field-cooled magnetization opens up at 25 K for $\text{Sr}_3\text{NiIrO}_6$ and at about 60 K in $\text{Sr}_3\text{CoIrO}_6$, close to the temperatures at which the coercive fields extrapolate to zero [*c.f.* Fig. 3(f)]. There is also a broad feature near 75 K in $\text{Sr}_3\text{NiIrO}_6$ and 110 K in $\text{Sr}_3\text{CoIrO}_6$. Comparable behavior was observed in earlier susceptibility studies of these materials^{13,15-17}; the characteristic temperatures at which the various features occur are very similar in the present paper and in all the previous work, suggesting that they are intrinsic to $\text{Sr}_3\text{NiIrO}_6$ and $\text{Sr}_3\text{CoIrO}_6$, and not due to variations in sample quality or preparation method. As noted in the Introduction, the broad

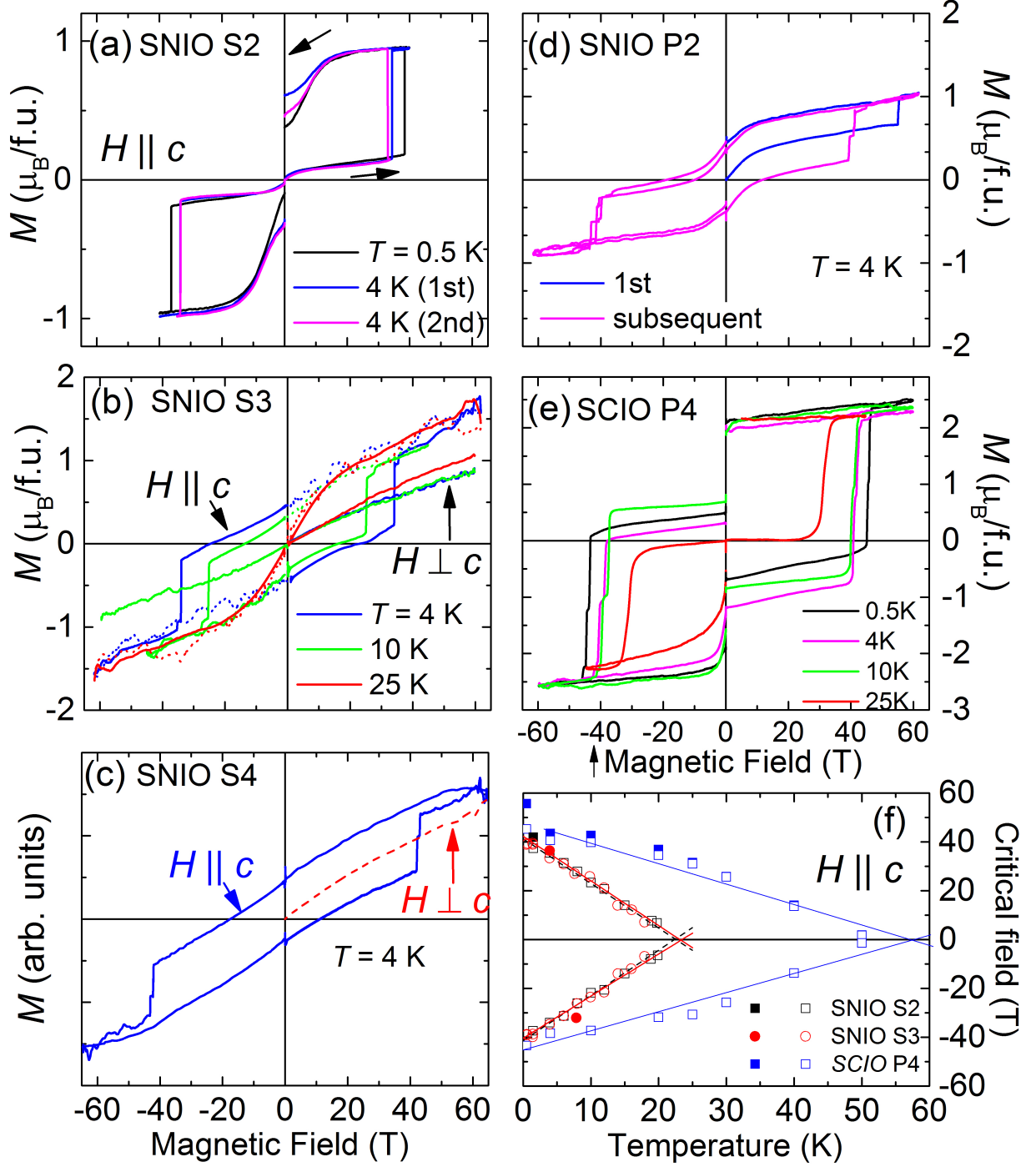


FIG. 3. Hysteresis loops and large coercive fields: (a-e) Magnetization M as a function of magnetic field $\mu_0 H$ of $\text{Sr}_3\text{NiIrO}_6$ (SNIO) and $\text{Sr}_3\text{CoIrO}_6$ (SCIO) measured in a series of pulses using a capacitor-bank-driven 65 T pulsed magnet. Sample numbers, field directions and measurement temperatures T are given in each section of the figure, where S refer to single crystals and P to polycrystals. The vertical jumps in M occur at the coercive field, $\mu_0 H_c$. Data in (b) and (c) are shown for $H \parallel c$ (hysteresis) and $H \perp c$ (no hysteresis). Magnetization units are shown as Bohr magnetons per formula unit, except in the case of (c), where the sample was destroyed in a pulsed-magnet failure before the calibration procedure detailed in Section II could be carried out. (f) T -dependences of the coercive magnetic fields are summarized for $\text{Sr}_3\text{NiIrO}_6$ samples S2 and S3, and $\text{Sr}_3\text{CoIrO}_6$ sample P4.

feature and subsequent rise in susceptibility correspond to the onset of disordered magnetism previously observed in neutron diffraction^{15,16}.

Figs. 4(c) and (d) show the DC magnetic susceptibility and the AC magnetic susceptibility at 10 Hz and 10 kHz for $\text{Sr}_3\text{NiIrO}_6$ and $\text{Sr}_3\text{CoIrO}_6$. The sharp jump in M already seen in Fig. 4(a) is observed also in the AC susceptibility data. However, the temperature at which the jump occurs is strongly dependent on the frequency of the applied magnetic field; between 10 Hz and 10 kHz it increases by about 50% in both compounds. A qualitatively similar shift of susceptibility features with measurement frequency was reported for $\text{Sr}_3\text{NiIrO}_6$ in Ref. 17.

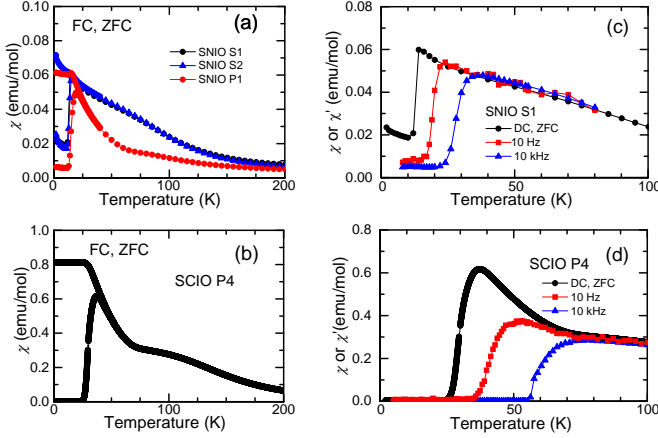


FIG. 4. Temperature-dependent magnetization: (a) and (b) Zero-field cooled (ZFC) and field-cooled (FC) magnetic susceptibility χ measured in a superconducting magnet as a function of temperature T in an applied field of 0.2 T for (a) $\text{Sr}_3\text{NiIrO}_6$ single-crystal samples S1 and S2 and polycrystalline sample P1 and (b) $\text{Sr}_3\text{CoIrO}_6$ polycrystalline sample P4. (c) and (d) AC magnetic susceptibility with a 10^{-3} T AC excitation at 10 Hz and 10 kHz, compared to DC magnetic susceptibility taken at 0.2 T for (c) $\text{Sr}_3\text{NiIrO}_6$ S1 and (d) $\text{Sr}_3\text{CoIrO}_6$ P4.

Though the changes in field are much smaller, the timescales spanned by the AC susceptibility data are similar to those of a field sweep in the 65 T short-pulse magnet (see Section II and Figure 2)³⁰. In Fig. 5 we therefore compare SQUID magnetization data taken using magnetic-field sweep rates of 0.008 T/s [Fig. 5(a)] with pulsed field magnetometry data employing sweep rates of up to 3.5 kT/s [Fig. 5(b)]; $\text{Sr}_3\text{NiIrO}_6$ polycrystalline sample P2 was used for these experiments, and the fields employed were kept well below the large coercive fields observed at low temperatures. Both data sets are plotted as differential susceptibility $dM(H, T)/dH$ on the initial rising field sweep following zero-field cooling. Note that for the slower superconducting magnet sweeps, the features observed correspond closely to those reported in Ref. 16 (*i.e.* an initial, relatively steep increase in $M(H)$ with increasing H , followed by a smaller

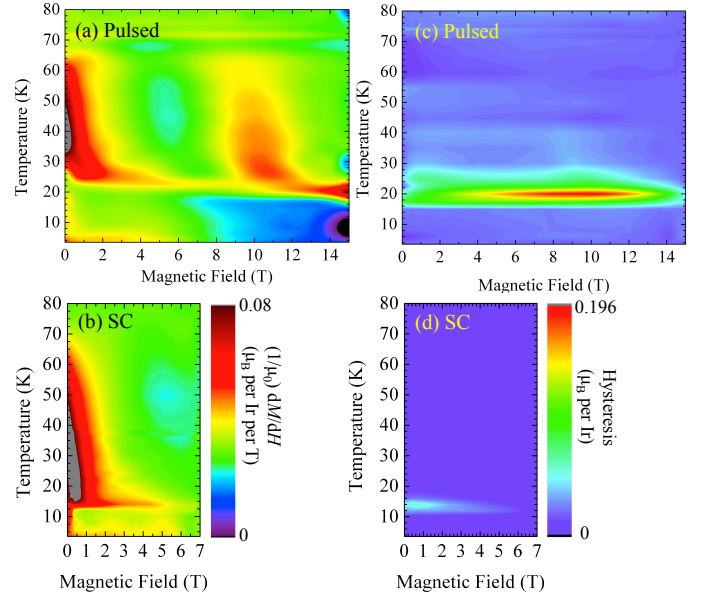


FIG. 5. Illustration of slow dynamics: the contour plots in (a) and (b) show dM/dH versus $\mu_0 H$ and T for $\text{Sr}_3\text{NiIrO}_6$ polycrystalline sample P2 in a pulsed magnetic field with a sweep rate ≈ 3500 T/s (a) and in a superconducting magnet (SC) with a magnetic field sweep rate of 0.008 T/s (b). Both (a) and (b) show data recorded on rising field sweeps. Corresponding plots of the hysteresis between falling and rising magnetic field sweeps, defined as $\text{hysteresis} = [M(H, T)_{\text{falling}} - M(H, T)_{\text{rising}}]$, are shown in (c) (pulsed field) and (d) (superconducting magnet - SC). The contour plots are based on field sweeps at constant temperatures spaced by 1–2 K for $T < 30$ K and ≈ 5 K for $T > 30$ K. Note that as the field sweep rate increases, features in dM/dH and regions of pronounced hysteresis are pushed to higher T .

gradient at higher fields). However, the much higher field sweep rates of the pulsed magnet shift the regions of large dM/dH to higher temperatures, analogous to the upward shift of the step in χ caused by increasing the frequency of the AC susceptibility measurement (Fig. 4)¹⁷.

Figs. 5(c) and (d) compare corresponding plots of the hysteresis in M between rising and falling magnetic field sweeps. Note that in the SQUID measurement, there is a small region of non-remanent hysteresis at fields well below the coercive field at corresponding temperatures (*c.f.* Fig. 3), previously noted in Refs. 15 and 16. As the field sweep rate increases (and therefore the timescale of the measurement decreases), the region of hysteresis is also pushed to higher T .

These slow dynamics are also evident in $\text{Sr}_3\text{CoIrO}_6$, as illustrated in Figure 6, which shows magnetization measured in a vibrating-sample magnetometer as a function of time after applying a field of 13 T. The magnetization varies on a timescale of hours, with the longest rise times occurring close to 20 K. A similar effect was previously observed in $\text{Sr}_3\text{NiIrO}_6$ [16].

The low-magnetic-field data shown in Figures 4, 5 and 6 show the magnetization exhibiting slow dynamics¹⁷ at

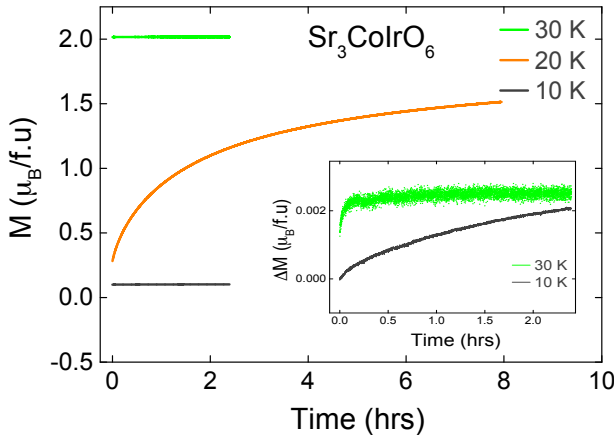


FIG. 6. Magnetization measured in a vibrating sample magnetometer as a function of time t after sweeping from 0–13 T at a rate of 0.01 T s^{-1} ; $t = 0$ is the time at which 13 T is reached. Data are shown for sample temperatures of 10, 20 and 30 K. The inset shows an enlargement of data from the main figure, plotted as $\Delta M = M(t) - M(0)$, where $M(0)$ is the magnetization at $t = 0$.

low temperatures. In each material studied here, the upper temperature limit of this behaviour is close to the temperature at which the coercive fields observed in the high-field experiments (Fig. 3) collapse to zero. Clearly, the high-field hysteresis loops are linked to the temperature region over which slow dynamics of the magnetization is observed (see Introduction and the discussion of Fig. 4 above).

C. Dependence on pulsed-field sweep rate and history

In view of the slow relaxation observed in the low-field magnetization described in the previous section, and the fact that pulsed magnetic fields are used for the high-field measurements, we investigate whether the hysteresis loops depend on the magnetic-field sweep rate. It is found that there is a small dependence on the sweep rate, which is varied between 25 and 10,000 T/s; to this end, Fig. 7 reviews $M(H)$ measurements of polycrystalline $\text{Sr}_3\text{NiIrO}_6$ sample P3 both in the 60 T Long-pulse Magnet and in the 65 T short-pulse magnet (see Fig. 2 for typical sweep rates). First, Fig. 7(a) displays a hysteresis loop measured in the 65 T short-pulse magnet, showing the initial upswing following zero-field cooling, and the subsequent hysteresis loop. Fig. 7(b) summarizes the coercive field H_c as a function of sweep rate in the different magnets, where H_c is determined from the steepest part of the jump in $M(H)$. Finally H_c is plotted for a series of magnetic field sweeps with varying sweep rate in Fig. 7(c). The coercive field values are measured in a sequence of alternating positive and negative field pulses denoted by *pulse number*; no other field pulses were applied and the sequence also includes two warmings of

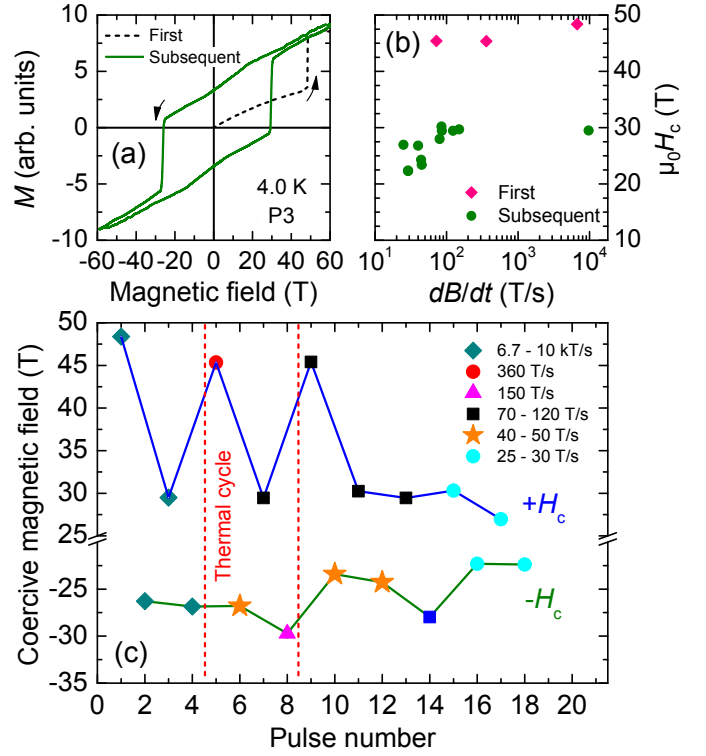


FIG. 7. Illustration of sweep-rate dependence of the coercive field for $\text{Sr}_3\text{NiIrO}_6$: (a) $M(H)$ data for polycrystalline sample P3 of $\text{Sr}_3\text{NiIrO}_6$ measured in the 65 T short-pulse magnet at $T = 4 \text{ K}$. Black dotted lines denote the initial pulse after zero-field cooling whilst the green solid line indicates data for subsequent pulses. (b) Sweep-rate dependence of coercive magnetic field ($\mu_0 H_c$). (c) History dependence of coercive magnetic field ($\mu_0 H_c$) under various sweep rates (plotted as a function of pulse number). For sweep rates larger than 360 T/s, the 65 T short-pulse magnet was used; other data were taken using the generator-driven 60 T Long-Pulse Magnet. Twice during this experiment, the sample was thermally cycled to room temperature and back down to $T = 4 \text{ K}$ (denoted by red vertical dashed lines).

the sample to room temperature, followed by zero-field cooling, denoted by vertical dashed red lines. The data again illustrate the previously mentioned finding that H_c is higher on the initial magnetic field sweep after zero-field-cooling. Following this initial pulse, the magnitude of the coercive field also depends on the direction of the field; it is smaller when the field is applied in the opposite direction to the initial pulse, and somewhat larger when the field is applied in the same direction. This asymmetry is bigger for polycrystalline samples. Moreover, a smaller stochastic variation of coercive field ($\sim 2 \text{ T}$) is frequently observed from pulse to pulse, even when the sweep rate and other conditions are kept the same. Taking all of these sample-history-dependent considerations into account, the data in Fig. 7(b) show that the coercive field tends to somewhat lower values as the sweep rate is decreased.

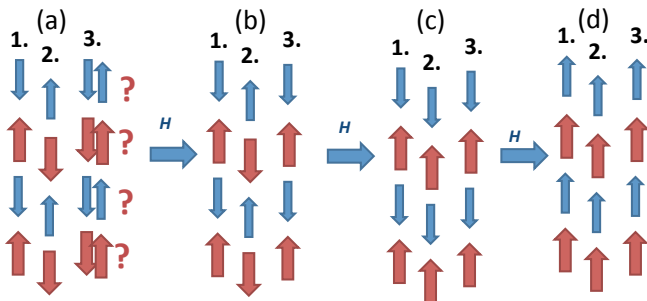


FIG. 8. Model for the behavior of the low-temperature magnetization $M(H)$ of $\text{Sr}_3\text{NiIrO}_6$. Red arrows represent the magnetic moments of the Ni^{2+} ions ($\approx 1.5\mu_B$) and blue arrows those of the Ir^{4+} ions ($\approx 0.5\mu_B$). (a) The PDA state at $H = 0$. This involves the moments of two ferrimagnetic c -axis chains (1, 2) being antiparallel to each other. The moments on the third chain (3) are disordered; this is represented by the question marks (?). (b) Increasing H from zero gradually orders the disordered chain (3), leading to an increase in M to a maximum possible value of $\frac{1}{3}\mu_B$ per formula unit. (c) At the coercive field H_c , the moments on one of the chains (2) flip (*i.e.* the transition is sharp), increasing M to $\approx \mu_B$ per formula unit. (d) At an (as yet inaccessible) even higher H , the system becomes ferromagnetic. Though the figure illustrates the situation in $\text{Sr}_3\text{NiIrO}_6$, similar physics will apply in the case of $\text{Sr}_3\text{CoIrO}_6$.

IV. DISCUSSION

In summary, we observe high-field hysteresis loops in single and polycrystalline samples of $\text{Sr}_3\text{NiIrO}_6$, and in polycrystalline samples of $\text{Sr}_3\text{CoIrO}_6$, exhibiting record coercive fields of up to 55 T. Despite the variation among samples, the presence of high-field transitions is robustly observed in all measured samples of $\text{Sr}_3\text{NiIrO}_6$ and $\text{Sr}_3\text{CoIrO}_6$. The hysteresis (*i.e.* memory of previous field pulses) is observed to create a remanent magnetization stable for up to 30 hours in all samples except one. The observed behavior strongly suggests that the magnetization jump at H_c is an intrinsic property of these compounds, with the sweep-rate and history dependences being caused by sluggish kinetics associated with the magnetic frustration intrinsic to this structural family^{6,17}; the same frustration is responsible for the slow magnetic relaxation (Figs. 4, 5) and the strong variation of the fall in M with frequency (Fig. 4). By contrast, in systems such as $(\text{Sm},\text{Sr})\text{MnO}_3$ [33], where the magnetization jumps are not intrinsic, but associated with quenched disorder, the smaller the field-sweep rate, the *larger* the field needed to realize the transition, the opposite of what we observe in $\text{Sr}_3\text{NiIrO}_6$ (Fig. 7).

We turn to a possible model for the hysteresis loops, starting from the PDA arrangement proposed^{15,16} for $\text{Sr}_3\text{NiIrO}_6$ and $\text{Sr}_3\text{CoIrO}_6$; the PDA state seems to us²⁶ to be the most likely explanation of neutron scattering and other data. Moreover, as detailed in the Introduction, PDA phases appear to be a rather general feature of the $\text{A}_3\text{BB}'\text{O}_6$ family. The PDA state thought to occur

in the title compounds involves the moments of two ferrimagnetic c -axis chains being antiparallel to each other, whilst the spins on a third chain are disordered at zero magnetic field; this situation is shown schematically for $\text{Sr}_3\text{NiIrO}_6$ in Fig. 8(a). We now examine what might happen to the three chains and their net magnetization as the field is increased.

Once the magnetic field increases from zero, we suggest that the moments on the disordered chain gradually align ferrimagnetically in the field; this would be responsible for the increasing magnetization seen below the coercive field (See Fig. 3). The *gradual* increase in M , and the somewhat variable shape of $M(H)$ for different samples will be due to the slow relaxation of a phase with magnetic frustration that is sensitive to small variations in disorder³². Taking the example of $\text{Sr}_3\text{NiIrO}_6$, neutron-scattering data^{15,16} are consistent with a moment of $1.5\mu_B$ on the Ni^{2+} ions and one of $0.5\mu_B$ on Ir^{4+} (see Introduction). Therefore, once the spins on the disordered chain have aligned [Fig. 8(b)], the maximum net moment per formula unit in $\text{Sr}_3\text{NiIrO}_6$ will be $\frac{1}{3}[2(1.5 - 0.5)\mu_B - (1.5 - 0.5)\mu_B] = \frac{1}{3}\mu_B$.

On further increasing the field, we propose that the moments on the remaining chain that is antialigned to the field flip [Fig. 8(c); see also the *Supplemental Material* section of Ref. 10]; we believe that this corresponds to the sharp jump in $M(H)$ seen at the coercive field. The “chain flip” should result in a net moment per $\text{Sr}_3\text{NiIrO}_6$ formula unit of $\frac{2}{3}(1.5 - 0.5)\mu_B = \mu_B$, or a jump in $M(H)$ of $\frac{2}{3}\mu_B$ on the first sweep up of the field after cooling (the jump will be doubled in height on going around the hysteresis loop).

The predicted value of the magnetization (μ_B per formula unit) just above the coercive field is in good agreement with the experimental values for $\text{Sr}_3\text{NiIrO}_6$ from Fig. 3. However, from sample to sample there is some variation between the amount of magnetization acquired prior to the coercive field and that gained at the step. It is possible that the “chain flip” transition [Fig. 8(c)] occurs in some samples before the field-induced derandomization of the disordered chain of the slowly relaxing phase is complete; once the flip does occur, it is likely that co-operative effects will drag any remaining disordered moments in the required direction.

Note that the Ni^{2+} and Ir^{4+} moments in individual chains remain antialigned after the “chain flip” transition at the coercive field [Fig. 8(c)]; there is still potential for a higher field to increase the magnetization of $\text{Sr}_3\text{NiIrO}_6$ to its saturated value of $\frac{3}{3}(1.5 + 0.5)\mu_B = 2\mu_B$, implying that another transition at even higher magnetic fields can be expected, when *all* the Ir and Ni moments align [Fig. 8(d)]. As mentioned above, a field of 92 T was insufficient to reach this transition.

The *Supplemental Material* section of Ref. 10 points out that each disordered chain can be surrounded by a variety of different configurations of ordered chains. This may be the reason why the first sweep of the magnetic field after cooling into the slowly relaxing phase results

in a higher coercive field; the field must overcome this stochastic spread of interchain interactions before the “chain flip” can be accomplished. Once the system is in the phase represented by Fig. 8(c), with its remanent moment, this disorder is removed and subsequent chain flips (in the hysteresis loop) can be driven by a lower field.

Fig. 8 uses the example of $\text{Sr}_3\text{NiIrO}_6$ to illustrate the field-induced changes; we believe that the same mechanism can account for the hysteresis loops observed in $\text{Sr}_3\text{CoIrO}_6$. Though the Co^{2+} ion carries a higher moment than Ni^{2+} (see Introduction), the coercive fields in the two materials are very similar, suggesting that the physics is driven by the Ir^{4+} ion³⁴.

PDA states of varying types have also been proposed for isostructural $\text{Ca}_3\text{Co}_2\text{O}_6$ [35 and 36], $\text{Sr}_3\text{Co}_2\text{O}_6$ [37], $\text{Ca}_3\text{CoRhO}_6$ [25], and $\text{Sr}_3\text{NiRhO}_6$ [23]. Just as in the title compounds of the current paper (see Introduction and Section IIIB), in these other materials the magnetic ordering sets in gradually as a function of temperature. This is suggested by broadened or absent signatures of the phase transition in the heat capacity versus temperature, despite evidence of magnetic ordering in elastic neutron scattering at low temperatures. We suggest that a similar mechanism to that proposed for $\text{Sr}_3\text{NiIrO}_6$ and $\text{Sr}_3\text{CoIrO}_6$ in the current paper, involving field-induced alteration of the PDA state, is responsible for the analogous magnetic hysteresis loops, sensitive to extrinsic parameters, that have been seen in these and other members of the $\text{A}_3\text{BB}'\text{BO}_6$ family: for example, at 4 K the coercive field of $\text{Ca}_3\text{Co}_2\text{O}_6$ is 7 T [38], that of $\text{Ca}_3\text{CoMnO}_6$ is 10 T [39], and that of $\text{Ca}_3\text{CoRhO}_6$ is 30 T [25]. Adding $\text{Sr}_3\text{NiIrO}_6$ and $\text{Sr}_3\text{CoIrO}_6$ from the current work ($\mu_0 H_c = 52 - 55$ T) to this series, it is apparent that the coercive field increases as the B' atom varies from 3d to 4d to 5d. The fact that the coercive fields in the $\text{A}_3\text{BB}'\text{BO}_6$ family become larger for the 5d iridate members suggests that the more exotic anisotropy associated with the spin-orbit entangled Ir^{4+} state plays a role¹⁰.

Remanent moments and hysteresis loops extending to somewhat smaller fields than those in the title compound have been observed in other oxides where disorder and/or frustration dominate the magnetic properties at low temperatures^{33,40,41}. As mentioned above, the hysteresis loops observed in the $(\text{Sm},\text{Sr})\text{MnO}_3$ system³³ depend on the field-sweep rate; the highest extent of the hysteresis loop observed was ≈ 4 T. $\text{Ca}_3\text{Co}_{2-x}\text{Mn}_x\text{O}_6$ ($x = 0.96$) contains frustrated ferromagnetic nearest-neighbor and antiferromagnetic next-nearest neighbor interactions^{40,41}; the coercive field is only about 2 T, but the elongated hysteresis loops are observed to extend to almost 13 T at low temperatures.

In traditional commercial ferromagnets^{42–44} such as $\text{Nd}_2\text{Fe}_{14}\text{B}$, hysteresis loops are caused by ferromagnetic domains that result from competition between the short-range exchange interactions that prefer parallel spin alignment, and the free-energy penalty of maintaining a

magnetic field in an extended region of space around the sample³¹. The effect of this competition is that the energy scale for switching magnetic domains can be orders of magnitude smaller than those of the nearest-neighbor ferromagnetic exchange interactions. This is reflected in the coercive fields, which even in the most robust members of the Sm-Co and Nd-Fe-B families^{42–44} are less than 2 T at low temperatures, despite large exchange energies manifested as ferromagnetic ordering temperatures $\sim 600 - 1000$ Kelvin. At cryogenic temperatures, magnetic hysteresis effects can extend to higher fields ≈ 10 T in other ferromagnets, such as the colossal magnetoresistance manganites, and in $\text{Li}_2(\text{Li}_{1-x}\text{Fe}_x)\text{N}$, Gd_5Ge_4 , Gd-doped CeFe_2 , LuFe_2O_4 , and $\text{Fe}_{1/4}\text{TaSe}_2$ [45–51]. Large coercive fields in such magnets are typically caused by magnetocrystalline anisotropy due to spin-orbit interactions⁴⁴.

Generally, the microscopic order in a traditional ferromagnet does not change significantly around the hysteresis loop as the domains merely change direction and/or the domain walls move^{31,44}. By contrast, the conventional phenomenology of ferromagnetic domains *cannot* be involved in the magnetic hysteresis of $\text{Sr}_3\text{NiIrO}_6$ and $\text{Sr}_3\text{CoIrO}_6$ (and other members of the $\text{A}_3\text{BB}'\text{BO}_6$ family) which are initially in some form of PDA state after zero-field cooling. Instead, their magnetic groundstate evolves with field to produce a sufficient moment to account for the jump in $M(H)$ at the coercive field^{15,16}.

V. CONCLUSION

In conclusion, we observed a notable macroscopic consequence of the unusual local state of 5d ions in oxygen cages: coercive magnetic fields of up to 55 T for $\mathbf{H} \parallel \mathbf{c}$ in $\text{Sr}_3\text{NiIrO}_6$ and 52 T in $\text{Sr}_3\text{CoIrO}_6$, to our knowledge record high coercive magnetic fields for any material. The hysteresis is a consequence of an evolving frustrated antiferromagnetic ground state of 3d and 5d ions, where the 5d ions exist in a state with strong spin-orbit entanglement¹⁰. Our observations could be a macroscopic manifestation of the effects of spin-exchange anisotropy.

VI. ACKNOWLEDGMENTS

This work is funded by the U.S. Department of Energy, Basic Energy Sciences program “Science at 100 Tesla”. The NHMFL Pulsed Field Facility is funded by the US National Science Foundation through Cooperative Grant No. DMR-1157490, the State of Florida, and the US Department of Energy. Work in the UK is supported by the EPSRC. P.A.G. and J.S. would like to thank the University of Oxford for the provision of visiting fellowships, which enabled much of the low-field data in this work to be acquired. We are grateful to Daniel Haskel for early communication of X-ray magnetic circular dichroism data²⁶ prior to publication. The work at

Rutgers was supported by the NSF under Grant number NSF-DMREF-1233349, and the work at Postech was

supported by the Max Planck POSTECH/KOREA Research Initiative Program (Grant number 2011-031558) through NRF of Korea funded by MEST.

- ¹ B. J. Kim, H. Ohsumi, T. Komesu, S. Sakai, T. Morita, H. Takagi, and T. Arima, *Science* **323**, 1329 (2009).
- ² D. Khomskii, *Transition Metal Compounds*, 1st ed. (Cambridge UP, Cambridge, UK, 2014).
- ³ S. Lovesey, D. Khalyavin, M. P., L. Chapon, and T. Qi, *J. Phys.: Condens. Matter* **24**, 496003 (2012).
- ⁴ G. Jackeli and G. Khaliullin, *Phys. Rev. Lett.* **102**, 017205 (2009).
- ⁵ J. Chaloupka, G. Jackeli, and G. Khaliullin, *Phys. Rev. Lett.* **105**, 027204 (2010).
- ⁶ H.-S. Kim, C. H. Kim, H. Jeong, H. Jin, and J. Yu, *Phys. Rev. B* **87**, 165117 (2013).
- ⁷ S. H. Chun, J.-W. Kim, J. Kim, H. Zheng, C. C. Stoumpos, C. D. Malliakas, J. F. Mitchell, K. Mehlawat, Y. Singh, Y. Choi, T. Gog, A. Al-Zein, M. M. Sala, M. Krisch, J. Chaloupka, G. Jackeli, G. Khaliullin, and B. J. Kim, *Nature Physics* **11**, 462 (2015).
- ⁸ K. A. Modic, T. E. Smidt, I. Kimchi, N. P. Breznay, A. Biffin, S. Choi, R. D. Johnson, R. Coldea, P. Watkins-Curry, G. T. McCandless, J. Y. Chan, F. Gandara, Z. Islam, A. Vishwanath, A. Shekhter, R. D. McDonald, and J. G. Analytis, *Nat. Comm.* **5**, 4203 (2014).
- ⁹ W. Witczak-Krempa, G. Chen, Y. B. Kim, and L. Balents, *Annu. Rev. Condens. Matter Phys.* **5**, 57 (2014).
- ¹⁰ E. Lefrancois, A.-M. Pradipto, M. M. Sala, L. C. Chapon, V. Simonet, S. Picozzi, P. Lejay, and R. Ballou, *Phys. Rev. B* **93**, 224401 (2016).
- ¹¹ H.-C. zur Loye, Q. Zhao, D. E. Bugaris, and W. M. Chance, *Cryst. Eng. Comm.* **14**, 23 (2012).
- ¹² T.N. Nguyen, D.M. Giaquinta and H.C. zur Loye, *Chem. Mater.* **6** 1642 (1994).
- ¹³ T. N. Nguyen and H. C. zur Loye, *J. Solid State Chem.* **117**, 300 (1995).
- ¹⁴ G. V. Vajenine, R. Hoffmann, and H.-C. zur Loye, *Chemical Physics* **204**, 469 (1996).
- ¹⁵ E. Lefrancois, L. C. Chapon, V. Simonet, P. Lejay, D. Khalyavin, S. Rayaprol, E. V. Sampathkumaran, R. Ballou, and D. T. Adroja, *Phys. Rev. B* **90**, 014408 (2014).
- ¹⁶ D. Mikhailova, B. Schwarz, A. Senyshyn, A. M. T. Bell, Y. Skourski, H. Ehrenberg, A. A. Tsirlin, S. Agrestini, M. Rotter, P. Reichel, J. M. Chen, Z. Hu, Z. M. Li, Z. F. Li, and L. H. Tjeng, *Phys. Rev. B* **86**, 134409 (2012).
- ¹⁷ D. Flahaut, S. Hebert, A. Maignan, V. Hardy, C. Martin, M. Hervieu, M. Costes, B. Raquet, and J. Broto, *Eur. Phys. J. B* **35**, 317 (2003).
- ¹⁸ K. E. Stitzer, A. E. Abed, J. Darriet, and H.-C. zur Loye, *J. Am. Chem. Soc.* **123**, 8790 (2001).
- ¹⁹ G. R. Zhang, X. L. Zhang, T. Jia, Z. Zeng, and H. Q. Lin, *J. Appl. Phys.* **107**, 09E120 (2010).
- ²⁰ S. Sarkar, S. Kanungo, and T. Saha-Dasgupta, *Phys. Rev. B* **82**, 235122 (2010).
- ²¹ X. Ou and H. Wu, *Scientific Reports* **4**, 4609 (2014).
- ²² S. Niitaka, H. Kageyama, M. Kato, K. Yoshimura and K. Kosuge, *J. Solid State Chem.* **146**, 137 (1999).
- ²³ N. Mohapatra, K. K. Iyer, S. Rayaprol, and E. V. Sampathkumaran, *Phys. Rev. B* **75**, 214422 (2007).
- ²⁴ M. Mekata, *J. Phys. Soc. Jpn.* **42**, 76 (1977).
- ²⁵ S. Niitaka, H. Kageyama, K. Yoshimura, K. Kosuge, S. Kawano, N. Aso, A. Mitsuda, H. Mitamura, and T. Goto, *J. Phys. Soc. Jpn.* **70**, 1222 (2001).
- ²⁶ D. Haskel, S. Chikara *et al.*, preprint (2016).
- ²⁷ B. J. Kim, H. Jin, S. J. Moon, J.-Y. Kim, B.-G. Park, C. S. Leem, J. Yu, T. W. Noh, C. Kim, S.-J. Oh, J.-H. Park, V. Durairaj, G. Cao, and E. Rotenberg, *Phys. Rev. Lett.* **101**, 076402 (2008).
- ²⁸ The Supplemental Information contains X-ray powder diffraction results for the $\text{Sr}_3\text{NiIrO}_6$ and $\text{Sr}_3\text{CoIrO}_6$ samples.
- ²⁹ P. Goddard, J. Singleton, P. Sengupta, R. D. McDonald, T. Lancaster, S. J. Blundell, F. L. Pratt, S. Cox, N. Harrison, J. L. Manson, H. I. Southerland, and J. A. Schlueter, *New. J. Phys.* **10**, 083025 (2008).
- ³⁰ J. Singleton, C.H. Mielke, A. Migliori, G.S. Boebinger and A.H. Lacerda, *Physica B* **346** 614 (2004).
- ³¹ B. D. Cullity and C. D. Graham, *Introduction to Magnetic Materials*, 2nd ed. (Wiley, 2009).
- ³² V. Kiryukhin, S. Lee, W. Ratcliff, Q. Huang, H. T. Yi, Y. J. Choi, and S.-W. Cheong, *Phys. Rev. Lett.* **102**, 187202 (2009).
- ³³ L.M. Fisher, A.V. Kalinov, I.F. Voloshin, N.A. Babushkina, D.I. Khomskii, Y. Zhang and T.T.M. Palstra, *Phys. Rev. B* **70**, 212411 (2004).
- ³⁴ Further justification for regarding the coercive field as a field-induced phase transition comes from the rough energy scales involved, obtained by multiplying the coercive field by half the switched moment: this gives ~ 10 meV, of the same order of magnitude as the energy scale associated with the magnetic ordering temperature $k_B T_1$ (75 K for $\text{Sr}_3\text{NiIrO}_6$ and 110 K for $\text{Sr}_3\text{CoIrO}_6$; see Introduction and Section III B).
- ³⁵ S. Agrestini, L. C. Chapon, A. Daoud-Aladine, J. Schefer, A. Gukasov, C. Mazzoli, M. R. Lees, and O. A. Petrenko, *Phys. Rev. Lett.* **101**, 097207 (2008).
- ³⁶ S. Agrestini, C. L. Fleck, L. C. Chapon, C. Mazzoli, A. Bombardi, M. R. Lees, and O. A. Petrenko, *Phys. Rev. Lett.* **106**, 197204 (2011).
- ³⁷ X. X. Wang, J. J. Li, Y. G. Shi, Y. Tsujimoto, Y. F. Guo, S. B. Zhang, Y. Matsushita, M. Tanaka, Y. Katsuya, K. Kobayashi, K. Yamaura, and E. Takayama-Muromachi, *Phys. Rev. B* **83**, 100410 (2011).
- ³⁸ V. Hardy, M. R. Lees, O. A. Petrenko, D. M. Paul, D. Flahaut, S. Hebert, and A. Maignan, *Phys. Rev. B* **70**, 064424 (2004).
- ³⁹ Y. J. Choi, H. T. Yi, S. Lee, Q. Huang, V. Kiryukhin, and S.-W. Cheong, *Phys. Rev. Lett.* **100**, 047601 (2008).
- ⁴⁰ Y. J. Jo, S. Lee, E. S. Choi, H. T. Yi, W. Ratcliff, Y. J. Choi, V. Kiryukhin, S. W. Cheong, and L. Balicas, *Phys. Rev. B* **79**, 012407 (2009).
- ⁴¹ J. W. Kim, Y. Kamiya, E. D. Mun, M. Jaime, N. Harrison, J. D. Thompson, V. Kiryukhin, H. T. Yi, Y. S. Oh, S.-W. Cheong, C. D. Batista, and V. S. Zapf, *Phys. Rev. B* **89**, 060404 (2014).

- ⁴² Stephen Russenschuck, *Field computation for accelerator magnets: analytical and numerical methods for electromagnetic design and optimization*, Chapter 4 (Wiley, Weinheim, 2010).
- ⁴³ K.H. Buschow and F.R. de Boer *Physics of magnetism and magnetic materials* (Kluwer, Boston, 2003).
- ⁴⁴ J.M.D. Coey, IEEE Trans. Magn. **47**, 4671 (2011).
- ⁴⁵ A. Jesche, R.W. McCallum, S. Thimmaiah, J.L. Jacobs, V. Taufour, A. Kreyssig, R.S. Houk, S.L. Bud'ko and P.C. Canfield, Nature Communications **5**, 3333 (2014)
- ⁴⁶ V. Hardy, D. Flahaut, M.R. Lees and O.A. Petrenko, Phys. Rev. B **70**, 214439 (2004).
- ⁴⁷ C. Autret, A. Maignan, C. Martin, M. Hervieu, V. Hardy, S. Hebert and B. Raveau, Appl. Phys. Lett. **82**, 4746 (2003).
- ⁴⁸ E. Morosan, H.W. Zandbergen, Lu Li, M. Lee, J.G. Checkelsky, M. Heinrich, T. Siegrist, N.P. Ong and R.J. Cava, Phys. Rev. B **75**, 104401 (2007)
- ⁴⁹ A. Haldar, K.C. Suresh and A.K. Nigam, Phys. Rev. B **78** 144429 (2008).
- ⁵⁰ Weida Wu, V. Kiryukin, H.-J. Noh, K.-T. Ko, J.-H. Park, W. Ratcliff, II, P.A. Sharma, N. Harrison, Y.J. Choi, Y. Horibe, S. Lee, S. Park, H.T. Yi, C.L. Zhang and S.-W. Cheong, Phys. Rev. Lett. **101**, 137203 (2008).
- ⁵¹ K.-T. Ko, K. Kim, S.B. Kim, J.-Y. Kim, B.I. Min, J.-H. Park, F.-H. Chang, H.-J. Lin, A. Tanaka and S.-W. Cheong, Phys. Rev. Lett. **107**. 247201 (2011).